PAPER

Check for updates

Synergistic enhancement of EM and CM in Ag/AZO thin films for high-performance SERS detection of R6G and methylparaben†

Trong Vo Huu, [iD] ab Vy Truong Tran Nhat, ab Mai Nguyen Xuan, ab Hang Nguyen Thi Ngoc, ab Long Nguyen Hoang, [iD] ab Tuan Dao Anh, ab Ke Nguyen Huu ab and Hung Le Vu Tuan [iD] *ab

In Surface-Enhanced Raman Scattering (SERS) analysis, enhancing the Raman signal is crucial and is primarily governed by two mechanisms: electromagnetic mechanism (EM) and chemical mechanism (CM). While the EM is well understood, gaining insight into the CM and its synergy with EM is crucial for optimizing SERS performance. In this study, CM effects were investigated through molecular adsorption and charge transfer (CT) processes using SERS substrates composed of silver nanoparticles (AgNPs) integrated with aluminium-doped zinc oxide (AZO) semiconductor thin films. AgNPs were synthesized *via* microwave irradiation and centrifugation, followed by incubation with Rhodamine 6G (R6G) and Methylparaben (MP) to enhance analyte adsorption. Adsorption behaviours were analysed using the Langmuir and Freundlich isotherm models. The analyte-loaded AgNPs were then combined with AZO thin films prepared by sputtering. These hybrid substrates not only generated electromagnetic "hot spots" to boost Raman signals *via* the EM but also facilitated CT, thereby enhancing signals through CM. A proposed CT mechanism between the substrate and analytes is also presented. The results demonstrate that the Ag/AZO SERS substrates exhibit a strong synergistic EM–CM effect, enabling the sensitive detection of R6G and MP at low concentrations, achieving enhancement factors (EFs) of 8.67×10^{10} (at 10^{-13} M) and 1.45×10^{6} (at 0.001 ppm or 6.58×10^{-9} M), respectively.

1. Introduction

Nowadays, various modern analytical techniques are widely employed for analysis and detection of low concentrations of toxic organic molecules that are illegally mixed in foods, pesticides, and pharmaceuticals. These techniques include High performance liquid chromatography (HPLC), High performance thin layer chromatography (HPTLC), and Gas chromatography mass spectrometry (GC-MS). While these methods offer high reliability and accuracy, they require complex and time-consuming sample processing. In addition, their complex experimental conditions and high equipment costs limit their ability to process large quantities of samples efficiently.[1] Meanwhile, Raman spectroscopy, especially surface enhancement Raman signal (SERS), is a highly sensitive and accurate analytical technique for studying molecular structures and detecting trace concentrations of molecules. This method offers several advantages including rapid analysis, fingerprinting capability, non-destructive testing, and simple sample

preparation.[2,3] As a result, SERS has been increasingly applied in various fields, such as biomedicine and trace analysis.[3]

The methyl ester of *p*-hydroxybenzoic acid (parabens) has been one of the most widely used preservatives in cosmetic products, food, and medicines for many years. It is considered a safe chemical due to its broad antimicrobial spectrum, resistance to hydrolysis in both hot and cold water, low acute and long-term toxicity, and lack of carcinogenic activity.[5,6] Parabens consist of a homologous group that includes methylparaben (MP), ethylparaben, propylparaben, butylparaben, heptylparaben, and benzylparaben. These compounds are often used in combination due to their synergistic effects.[7] Due to its low toxicity and widespread use, MP is found in many everyday products such as toothpaste, deodorants, beauty creams, sunscreen filters, and bath gels.[8] However, excessive use of MP in high concentrations by some manufacturers has raised concerns about its harmful effects on human health. Studies have shown that MP can accumulate in the epidermis and affect keratinocytes, particularly under ultraviolet (UV) radiation from sunlight.[5] Additionally, MP has been found to bind to estrogen receptors, which has been linked to the development of human breast tumors.[4] Furthermore, MP poses an increasing threat to aquatic organisms as it is easily released into water systems through human waste and residual products.[8] Therefore, the

aUniversity of Science, Ho Chi Minh City, Vietnam. E-mail: lvthung@hcmus.edu.vn
bVietnam National University, Ho Chi Minh City, Vietnam
† Electronic supplementary information (ESI) available. See DOI: https://doi.org/10.1039/d5ra01381j

detection of MP residual in the aforementioned products is necessary for human health safety.

In SERS technique, Raman signal enhancement is crucial and primarily relies on two mechanisms: the electromagnetic mechanism (EM) and the chemical enhancement mechanism (CM). The EM is the dominant mechanism in SERS and is based on the localized surface plasmon resonance (LSPR), which enhances the electric field when the incident laser irradiates the substrate. LSPR typically occurs in noble metal nanoparticles such as Au, Ag, and Cu, particularly at nanoscale edges, tips, or crevices. Additionally, some transition metals like Pt, Ru, Fe, Co, and Ni have also been reported to enhance Raman signals. Noble metals exhibit high enhancement factors (EF) in the range of 10^6–10^8,[3,4] owing to forming nanostructures with "hot spots". Therefore, the optimization of these hot spots is crucial for substantially amplifying the Raman signal from the SERS substrate. Although the EM dominates the enhancement effect in SERS substrates based on noble metal nanoparticles, the contribution of the CM is indispensable and cannot be overlooked. The CM involves mechanisms such as molecular resonance, Mie resonance, exciton resonance, and, most notably, charge transfer (CT). When molecules are adsorbed onto the metal nanoparticle surface, the Fermi energy level of the nanoparticle aligns between the HOMO and LUMO energy levels of the molecules, facilitating charge transfer as an intermediate energy level.[10]

With the advancement of nanotechnology, an increasing number of semiconductor materials such as ZnS, TiO_2, Cu_2O, CuO, and ZnO are being studied and utilized as SERS substrates to replace noble metal nanoparticles. The CM plays a significant role in enhancing Raman signals in semiconductors. It is closely associated with charge transfer (CT) processes and exciton resonance. The effectiveness of the CM effect strongly depends on the type of molecules involved and the properties of the material substrates. Although semiconductors typically exhibit lower EF, around around 10–10^3, they serve as an excellent platform for shaping metal nanoparticles. This opens up the possibility of fabricating hybrid SERS substrates that combine semiconductors with noble metal nanoparticles to significantly enhance Raman signals. Examples of such hybrid structures include Ag–TiO_2, Ag–ZnO, Au–ZnO, and Ag–Si.[5–10] The hybrid SERS substrates combining semiconductors and noble metal nanoparticles offer outstanding advantages, such as easy controllability, increased nanoparticle density in "hot spots" clusters, a large effective surface area, and light trapping effects when laser irradiation is applied on the substrates (especially in structures like nanorods, nanotubes, nanoflowers…). These structures significantly increase the great role of CM in SERS, while also promoting the synergy between EM and CM in enhancement Raman signal.[11–13] When studying CM, many issues remain unclear explained and need further clarification. The CM often depends on chemical nature of probe molecules and involves the selective binding of molecules to the SERS surface. Therefore, investigating CM including the role of absorption between adsorbed molecules with SERS substrates, the role of CT in noble metals, semiconductors, and molecules, as well as its synergy with EM, is essentials.[14–19]

Considering the SERS mechanisms introduced above, our objective is to develop a hybrid SERS substrate to investigate CM and its synergy with EM, aiming to achieve the maximum possible enhancement factor for detecting organic analytes at ultra-low concentrations. Distinct from our previous study utilizing sputtered Ag on AZO substrates,[20] this work employs AgNPs synthesized via a microwave-assisted method combined with centrifugation followed by incubation with Rhodamine 6G (R6G) and MP, to enhance analyte adsorption compared to sputtering. Enhanced adsorption of these analytes onto the Ag nanoparticles promotes stronger interaction for improved Raman signals, and the adsorption behaviour was further analysed using the Langmuir and Freundlich isotherm models. The analyte-loaded AgNPs were then combined with AZO thin films prepared by sputtering. These hybrid substrates not only increase the density of AgNPs-induced hot spots to boost Raman signals via the EM but also facilitated CT, thereby enhancing signals through CM. A proposed CT mechanism between R6G, MP and Ag/AZO substrate is also presented.

2.   Experimental

Silver nitrate ($AgNO_3$, > 99.8%, CAS 7761-88-8) and sodium citrate ($Na_3C_6H_5O_7$,> 99.5%, CAS code 6132-04-3) were purchased from Fisher, R6G ($C_{28}H_{31}N_2O_3Cl$, 99%, CAS code 989-38-8) was bought from Biosynth, The MP (99.9%) was purchased from Institute of Drug Quality Control Ho Chi Minh city–IDQC HCMC.

In this study, Ag/AZO SERS substrates were fabricated using multiple methods. ZnO and AZO thin films were prepared via the sputtering method, while AgNPs were synthesized using the microwave-assisted centrifugal method.

First, glass slides were pre-treated by immersing them in 20% NaOH solution for 30 minutes. After that, they were ultrasonically cleaned in the following sequence: distilled water, acetone, distilled water, methanol, and distilled water, with each step lasting 15 minutes. Finally, the slides were immersed in ethanol for preservation. The treated glass slides were then used to fabricate Ag/AZO SERS substrates, following the procedure illustrated in Fig. 1 below.

2.1.   Preparation of AgNPs and molecules solution

To fabricate AgNPs capable of enhancing SERS signals via both EM and CM, we selected a microwave-assisted synthesis method followed by centrifugation to obtain spherical Ag nanoparticles with high uniformity.

Step 1: preparing AgNPs colloids by microwave and centrifugation method

The concentration of $AgNO_3$ solution greatly affects the size of AgNPs due to the interaction between Sodium citrate (SC) and $AgNO_3$.[21,22] In this study, the $AgNO_3$ solution concentration was varied at 30 mM, 40 mM, 50 mM, 60 mM, and 70 mM, while the SC concentration was maintained at a constant 44 mM.

First, to prepare 20 ml of $AgNO_3$ solution at different concentrations, the required masses of $AgNO_3$ must be
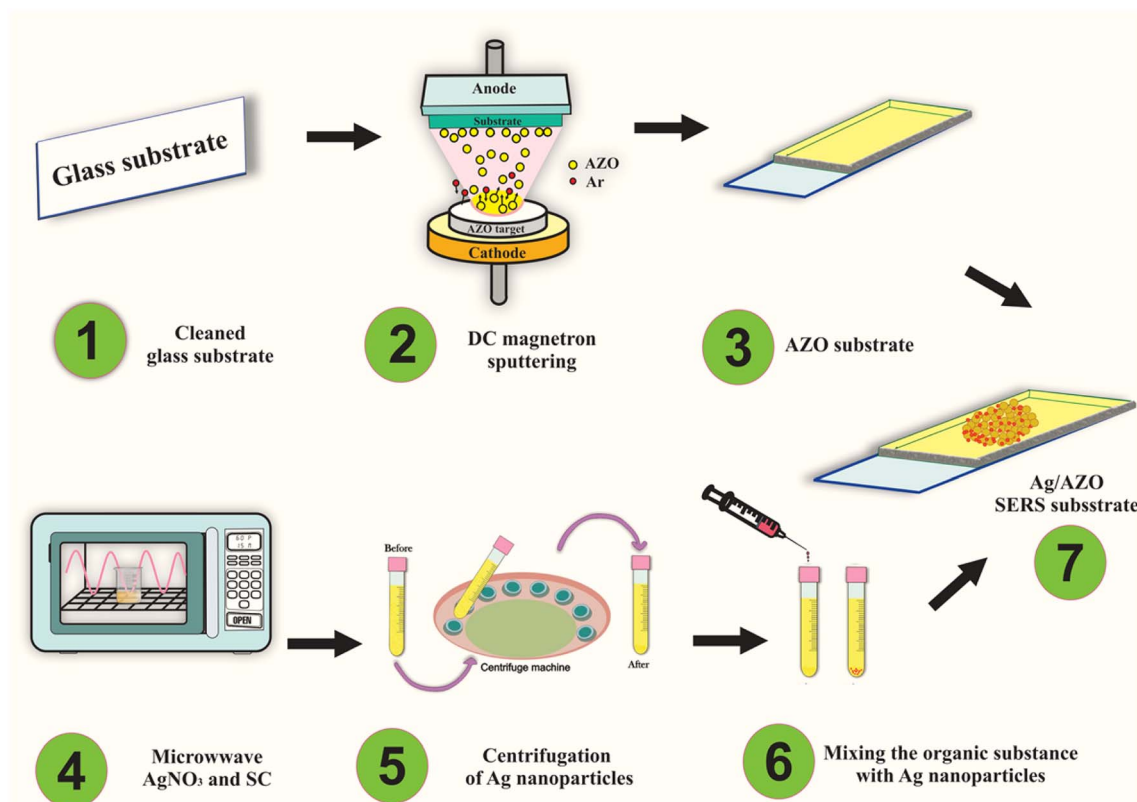
Fig. 1 Method for preparing Ag/AZO SERS substrates.

calculated, for example the mass need for a solution of concentration $C_M = 50$ mM is calculated as follow:

$$C_M = \frac{n_{SC}}{V_{SC}} = \frac{m_{SC}}{M_{SC} \times V_{SC}}$$
$$\Rightarrow m_{SC} = C_M \times M_{SC} \times V_{SC}$$
$$= 50 \times 10^{-3} \times 16\,987.20 \times 10^{-3} = 0.16787 \text{(g)} \quad (1)$$

Calculate similarly with other samples with concentrations of 30 mM, 40 mM, 60 mM, and 70 mM.
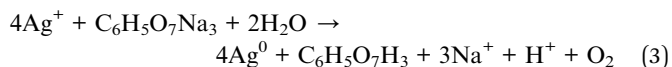
Second, to prepare 20 ml of SC with concentration $C_M = 44$ mM, its mass is calculated as follow:

$$C_M = \frac{n_{SC}}{V_{SC}} = \frac{m_{SC}}{M_{SC} \times V_{SC}}$$
$$\Rightarrow m_{SC} = C_M \times M_{SC} \times V_{SC}$$
$$= 44 \times 10^{-3} \times 25\,806.20 \times 10^{-3} = 0.227 \text{(g)} \quad (2)$$

Mix 99 ml of distilled water with 0.5 ml of prepared SC and 0.5 ml of prepared AgNO₃ solution. Stir the above mixture for 15 minutes. Then, put the above mixture in the microwave at 60 W in 10 minutes. In the microwaves, the reduction of Ag⁺ to Ag⁰ takes place according to the following equation:

$$4Ag^+ + C_6H_5O_7Na_3 + 2H_2O \rightarrow$$
$$4Ag^0 + C_6H_5O_7H_3 + 3Na^+ + H^+ + O_2 \quad (3)$$

After that, a yellow AgNPs colloid is obtained. Remove it and allow it to cool at room temperature. Transfer the AgNPs colloid into an eppendorf tube, and use a micropipette to extract 1000 μL from each tube. Then, centrifuge at 10 000 rpm for 10 minutes. After centrifugation, the AgNPs settle at the bottom of the eppendorf tube. Use a micropipette to remove 980 μL of the supernatant, leaving 20 μL of concentrated AgNPs in the tube (Table 1).

Step 2: preparing analyte solutions with different concentrations

Solutions of R6G and MP with a concentration of $C_{ppm} = 1000$ ppm in 20 ml are prepared as follows:

$$C_{ppm} = \frac{m_{molecule}}{m_{molecule} + m_{H_2O}} \times 10^6 = \frac{m_{molecule} \times 10^6}{m_{molecule} + D_{H_2O} \times V_{H_2O}}$$

$$\Rightarrow m_{molecule} = \frac{C_{ppm} \times D_{H_2O} \times V_{H_2O}}{10^6 - C_{ppm}} = \frac{1000 \times 1 \times 20}{10^6 - 1000}$$

$$= \frac{1000 \times 1 \times 20}{10^6 - 1000} = 0.0202 \text{ (g)} \quad (4)$$

Mix the analyte solution with distilled water and stir using a magnetic stirrer for 15 minutes. Repeat this process for solutions with concentrations lower than 1000 ppm, including 100 ppm, 10 ppm, 1 ppm, 0.1 ppm, 0.01 ppm, and 0.001 ppm.

Step 3: mixing the analyte solution with the AgNPs

Mix the AgNPs with 20 μL of the prepared analyte solutions. This process enables the formation of the desired ligand-AgNPs

Table 1 Parameters of synthesizing AgNPs colloid using microwave and centrifugation methods

Sample	AgNO$_3$ concentration	Na$_3$C$_6$H$_5$O$_7$ concentration	Microwave power	Microwave time
Ag30	30 mM	44 mM	60 W	10 minutes
Ag40	40 mM			
Ag50	50 mM			
Ag60	60 mM			
Ag70	70 mM			

system. Then, drop this solution onto the prepared glass, ZnO and AZO substrates to conduct Raman measurements.

2.2. Fabricate AZO substrate by magnetron DC sputtering

In this study, AZO (Al$_2$O$_3$ with 2% doped ZnO) thin films were fabricated using DC magnetron sputtering from AZO targets. According to our previous studies, doping Al$_2$O$_3$ at a concentration of 2% is optimal for the conductivity of the AZO semiconductor.[12] Additionally, a sputtering time of 45 minutes creates a rough AZO surface, enhancing the adhesion of nanoparticles. The sputtering process is illustrated in Fig. 1.

2.3. Material characterization

The properties and performance of the prepared materials were characterized as follows. Crystal structure of the AgNPs and Ag/AZO substrates were investigated using X-ray powder diffraction (Bruker AXS D8 Advance) employing CuK$_\alpha$ radiation ($\lambda = 1.541$ Å). Morphological details, including the size and shape determination of the synthesized AgNPs, along with surface and cross-sectional imaging of the AZO substrates, were examined by field-emission scanning electron microscopy (FE-SEM; Hitachi S4800). Optical characteristics were analyzed using UV-vis absorption spectroscopy (Halo RB-10)
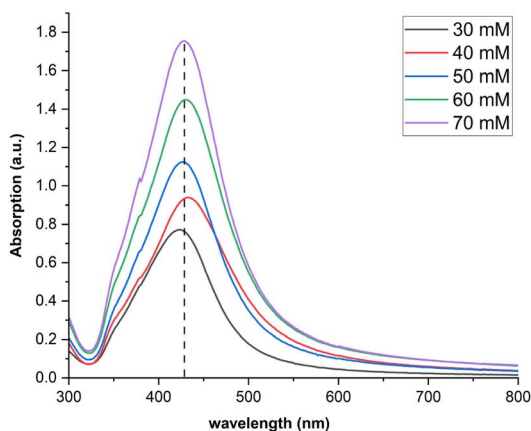
and Photoluminescence (PL) spectroscopy (Cary Eclipse-MY2246CG04, $\lambda_{ex} = 250$ nm). The surface wettability of the AZO substrates was assessed *via* contact angle measurements. Finally, the SERS performance was assessed by measuring the signal enhancement for R6G and MP analytes using a Horiba XploRa PLUS Raman system. These Raman measurements utilized a 532 nm laser excitation source operating at 1.5 mW power, focused to a spot diameter of 2 μm on the sample surface. The Raman spectrometer was calibrated prior to measurement using the Silicon peak at 520 cm^{-1}. Spectra were acquired over 4 seconds with 2 accumulations, employing a filtered laser intensity of 1%.

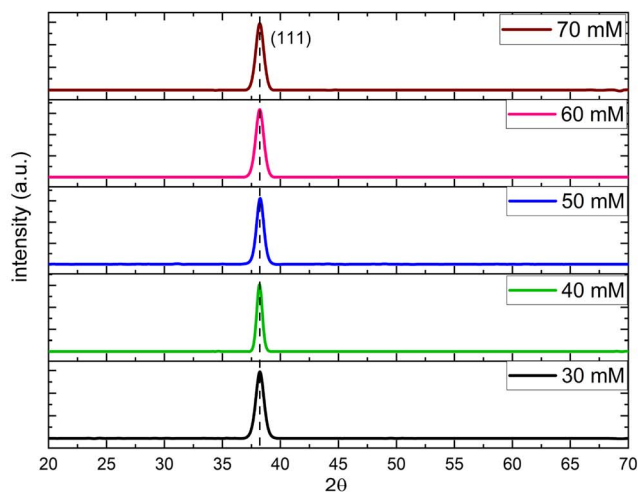## 3. Results and discussions

3.1. Characterization of AgNPs

Initially, the optical properties of AgNPs, prepared using various initial concentrations of AgNO$_3$, were examined. Fig. 2a presents the UV-vis spectra of samples at different AgNO$_3$ concentrations, all exhibiting strong plasmon resonance peaks. As the AgNO$_3$ concentration increases from Ag30 to Ag70, the plasmon peaks become more intense and sharper. All peaks appear in the wavelength range of 420–450 nm, confirming the formation of AgNPs. The symmetrical and narrow plasmon resonance bands indicate a uniform spherical shape and a narrow size distribution of nanoparticles.[23] The symmetry improves from Ag30 to Ag50 but gradually declines from Ag50 to Ag70, suggesting that sample Ag50 has the most uniform AgNPs with the narrowest size distribution.

Fig. 2b presents the XRD patterns of AgNPs at different concentrations on a glass substrate. The fabricated samples exhibit a distinct, high, and sharp (111) peak at a diffraction angle of $2\theta = 38.22°$, confirming that the samples possess a face-centered cubic (fcc) structure (JCPDS 4-783).[23] Table S1† shows that increasing the concentration from Ag30 to Ag70

Fig. 2 (a) UV-vis spectra of AgNPs colloids at varying AgNO$_3$ concentrations, (b) the XRD patterns of AgNPs at different concentrations on a glass substrate.
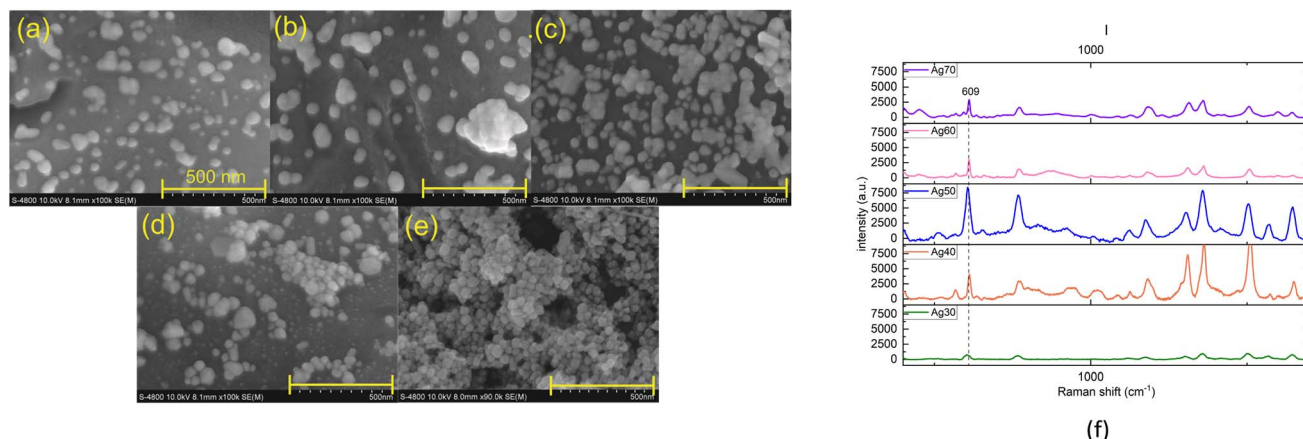
Fig. 3 SEM image of AgNPs. (a) Ag30; (b) Ag40; (c) Ag50; (d) Ag60; (e) Ag70; (f) Raman spectrum of the analyte R6G (10^{-6} M) adsorbed onto Ag30, Ag40, Ag50, Ag60, and Ag70 nanoparticles on a glass substrate.

results in an increase in the crystallite size of Ag nanoparticles from 92 Å to 139 Å.

Among the samples, Ag50 exhibits a well-defined crystal structure, optimal crystallite size, and the highest uniformity, making it the most suitable choice for SERS substrates.

The SEM images in Fig. 3 reveal that AgNPs in all samples exhibit a spherical shape, with particle sizes ranging from 40 to 60 nm, which is suitable for LSPR. The nanoparticle density increases as the AgNO$_3$ concentration rises from Ag30 to Ag70. While the nanoparticle density in samples Ag30 and Ag40 (Fig. 3a and b) is relatively low, the nanoparticles in samples Ag60 and Ag70 (Fig. 3d and e) tend to form dense agglomerations. Among them, sample Ag50 (Fig. 3c), with an average particle size of approximately 50 nm, demonstrates the best uniformity and optimal nanoparticle distribution on the substrate.

The phenomenon of AgNPs agglomeration with increasing AgNO$_3$ concentration can be explained as follows: Higher AgNO$_3$ concentrations enhance the availability of Ag$^+$ ions, leading to the formation of more nucleation sites. This, in turn, increases the interaction between Ag$^+$ ions and Ag seeds, resulting in larger crystallite sizes. At excessively high AgNO$_3$ concentrations, the small crystallites formed tend to aggregate into larger particles. Consequently, the size uniformity of the nanoparticles decreases, leading to instability in the SERS signal. This finding is consistent with the UV-vis spectra and XRD patterns discussed above.

The Raman spectra of 20 μL R6G at 10^{-6} M mixed with AgNPs of sample Ag50 are presented in Fig. 3f. The Raman spectra indicate that the Ag nanoparticles synthesized in the Ag50 sample exhibit the highest peak intensities.

3.2. Adsorption of R6G and MP on AgNPs surface

3.2.1. Determine the adsorption isotherm. To investigate the interaction between the organic molecules and the AgNPs, the Langmuir and Freundlich adsorption isotherm models were employed to study the adsorption behavior of the two analytes, R6G and MP.[24,25]

The Langmuir' s isotherm adsorption eqn (5). :

$$q_e = q_m \frac{k_L \times C_e}{1 + k_L C_e} \tag{5}$$

or expressed in linear form (eqn (6)):

$$\frac{C_e}{q_e} = \frac{1}{k_L q_m} + \frac{C_e}{q_m} \tag{6}$$

where C_e is the concentration of adsorbate solution (mg L^{-1}) after adsorption equilibrium, q_e is the adsorption capacity of the sample (mg g^{-1} dry adsorbent), q_m is the saturated adsorptive capacity (mg g^{-1}), k_L is the Langmuir' s adsorption coefficient (L mg^{-1}).

The Freundlich's isotherm adsorption eqn (7):

$$\ln q_e = \ln k_f + \frac{1}{n} \ln C_e \tag{7}$$

where k_f is the Freundlich constant (mg g^{-1}) and 'n' the Freundlich exponent.

The adsorption capacity of R6G and MP on AgNPs surface is measured by UV-vis spectroscopy. Measuring and calculating q_e and c_e from eqn (6) and (7) are carried out as follows:

First, build a calibration curve of analyte molecules: weigh 1 mg of analyte molecule powder and dissolve it in 10 mL of distilled water to obtain a 10 ppm solution. Dilute the 10 ppm solution with distilled water in appropriate proportions to obtain solutions with concentrations of 7.5, 5, 2.5, and 1 ppm (initial concentration C_0). Then take 2 mL of each solution, transfer it into a cuvette, and measure the absorption spectrum. After that, using the obtained data, plot a calibration curve based on the relationship between analyte concentration and absorption intensity.

Second, determine saturation absorption threshold concentration (C_e). During the adsorption process, analyte molecules bind to the AgNPs surface, leading to a gradual decrease in the solution concentration over time. By measuring the decrease in absorbance of the solutions and comparing it with calibration curve, the solution concentration after adsorption can be determined. Add 2 ml of AgNPs solution to 1 ml of analyte

solution. Measure the absorption spectrum of the solution at intervals of 10, 20, 30, 40, 50, 60, 70 minutes, then record the results. Compare the absorption intensity over time with the calibration curve to determine the decrease in concentration and the solution concentration after adsorption (C/C_0). When (C/C_0) no longer changes, the adsorption process has reached equilibrium. Record the equilibrium concentration C_e (mg l^{-1}). The adsorption capacity of the sample q_e (the amount of absorbent adsorbed per unit mass (mg g^{-1})) is calculated using the following formula:

$$q_e = \frac{(C_0 - C_e) \times V}{m} \quad (8)$$

where C_0 is the initial concentration (mg l^{-1}). V is the volume of adsorbed analyte solution (l). m is the mass of adsorbent AgNPs (g).

3.2.2. The adsorption of R6G. Based on the experimental steps described in Section 3.2.1, the calibration curve of analyte molecules (R6G) was obtained by measuring the absorption spectra of five solutions with concentrations of 10, 7.5, 5, 2.5, and 1 ppm, as shown in Fig. 4 and (Table 2).

The correlation coefficient (R^2) for the adsorption of R6G in Langmuir's isotherm is 0.99, while in Freundlich's isotherm, it is 0.91 (in Fig. 5). This indicates that the adsorption of R6G on the AgNPs surface follows Langmuir's isotherm, which applies to monolayer adsorption, where only a single layer of molecules is adsorbed onto the AgNPs surface. In monolayer adsorption, all adsorbed molecules are in direct contact with the adsorbent.[26,27] The monolayer adsorption of R6G molecules fits the Langmuir isotherm model. This can be attributed to cationic R6G readily interacting via electrostatic forces with the negatively charged AgNPs (due to adsorbed citrate COO- groups from synthesis). This strong interaction enhances R6G-AgNP binding and directly affects the Raman spectrum through the CM.[28,29]

Table 2 The coefficients C_e and q_e are determined from the absorption spectrum of R6G
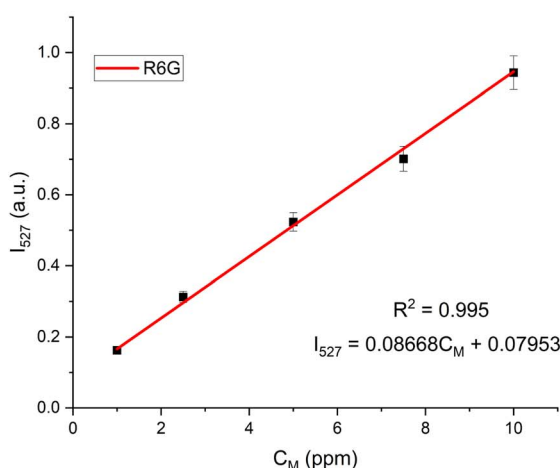
Concentration C_0 (ppm)	C_e (ppm)	q_e (µg g^{-1})	C_e/q_e (g l^{-1})	ln C_e	ln q_e
10	3.423	0.038	89.151	1.231	−3.260
7.5	1.836	0.033	55.526	0.608	−3.409
5.0	0.765	0.025	30.942	−0.268	−3.700
2.5	0.254	0.013	19.372	−1.370	−4.334
1	0.114	0.005	22.040	−2.172	−5.264

3.2.3. The adsorption of MP. MP serves as the analyte in this investigation. To study its adsorption onto Ag nanoparticles (NPs), the decrease in MP concentration following incubation with the AgNPs was monitored via absorption spectroscopy. Initially, a concentration calibration curve for MP was established. The calibration curve was obtained by measuring the absorption spectra of five solutions with concentrations of 10, 7.5, 5, 2.5, and 1 ppm, as shown in Fig. 6.
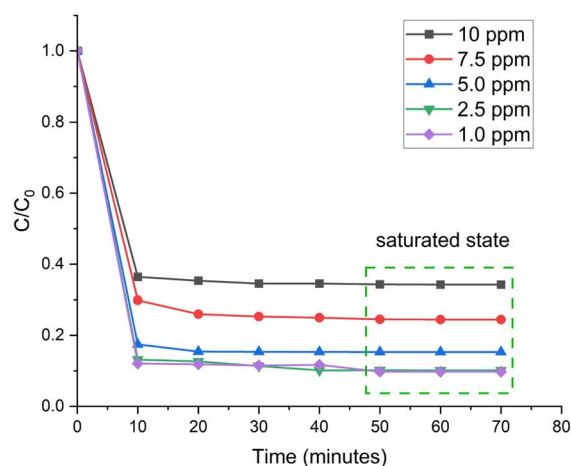
Fig. 6 illustrates the variation in relative concentration (C/C_0) over time (10–70 min) during the adsorption of MP on AgNPs at 50 mM for different initial MP concentrations, until the change reaches a saturated state. At this point, C_e of MP is determined, as shown in Table 3. The adsorption capacity (q_e) of the sample is calculated using eqn (8), and the obtained results are presented in the following tables.

Based on the results in the table above, the graphs illustrating the relationship between C_e and q_e according to Langmuir's and Freundlich's isotherms, as described in eqn (2) and (3), are presented (Fig. 7).

The correlation coefficient (R^2) for the adsorption of MP in Langmuir's isotherm is 0.95, while in Freundlich's isotherm, it is 0.99. This indicates that the adsorption of MP on the AgNPs

a)

b)

Fig. 4 (a) The calibration curve of R6G, (b) the variation in relative concentration (C/C_0) over time during the adsorption of R6G on AgNPs at 50 mM for different initial R6G concentrations.
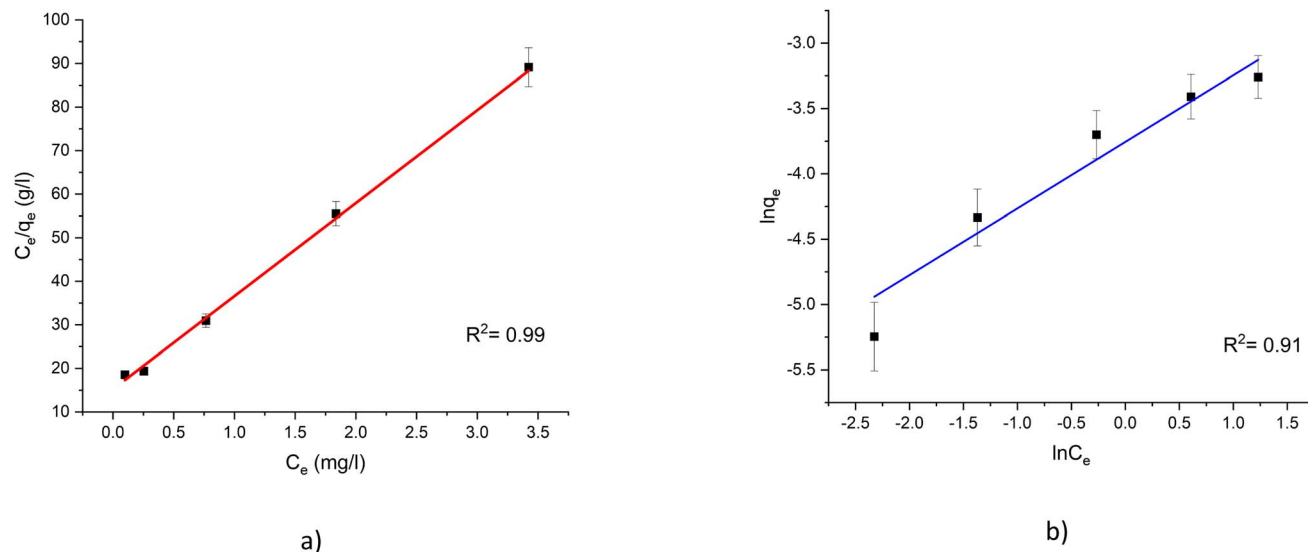
Fig. 5 (a) Graphs showing the relationship between C_e and q_e based on Langmuir's isotherm for R6G. (b) Graphs showing the relationship between C_e and q_e based on Freundlich's isotherm for R6G.
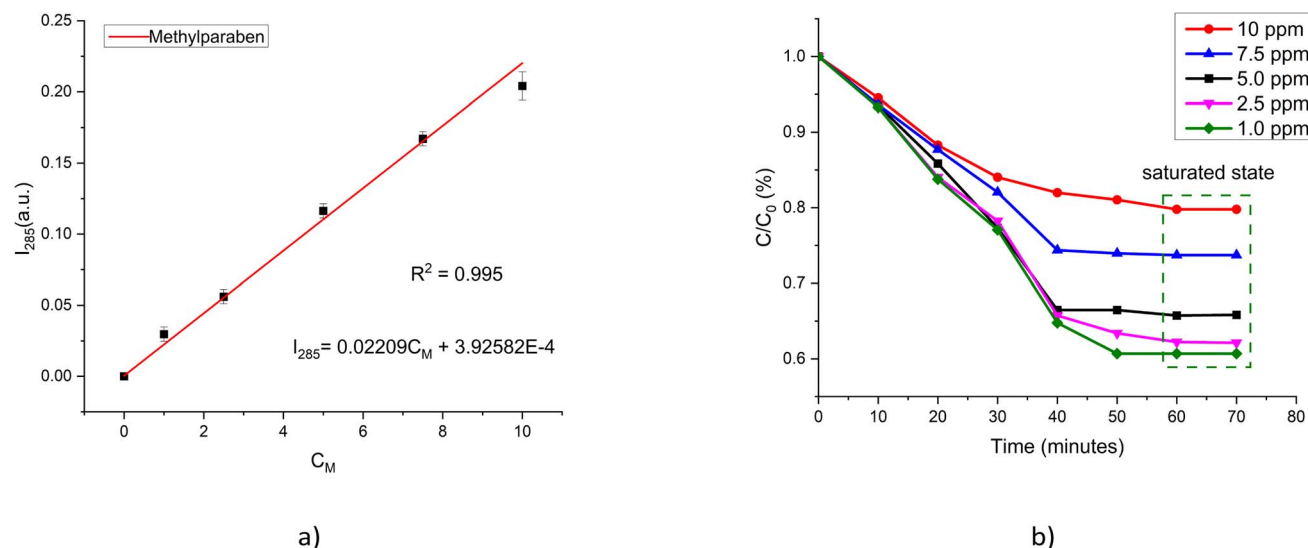

Fig. 6 (a) The calibration curve of MP, (b) the variation in relative concentration (C/C_0) over time during the adsorption of MP on AgNPs at 50 mM for different initial MP concentrations.

surface follows Freundlich's isotherm, which applies to multi-layer adsorption with adsorption sites of varying affinities. In multilayer adsorption, not all molecules are in direct contact with the adsorbent.[26,27] As a result, multilayer adsorption is generally weaker than monolayer adsorption.

MP adsorption onto the AgNPs surface mainly relies on weaker interactions like van der Waals forces, or potentially interactions between oxygen atoms (in the ester –COO– or hydroxyl –OH groups, if present after hydrolysis) and the Ag surface. This interaction is typically weaker and less specific than the electrostatic attraction of R6G. Due to weaker and less directional interactions, MP may adsorb in a less ordered

manner. At sufficiently high concentrations, it can potentially form molecular multilayers. Its adsorption process might better fit the Freundlich' s isotherm model, which describes adsorption on heterogeneous surfaces or multilayer adsorption. Thus, MP generally has a weaker affinity for the AgNPs surface than R6G. This weaker adsorption is one of the key reasons why the enhanced Raman signal of MP is lower than that of R6G.

3.3. Characterization of AZO substrate

3.3.1. Structure and morphology of substrate. In this section, the structural properties and surface morphology of the AZO substrate, fabricated *via* sputtering, were characterized.

Table 3 The coefficients Ce and qe are determined from the absorption spectrum of MP

Concentration C_0 (ppm)	C_e (mg l^{-1})	q_e (μg g^{-1})	C_e/q_e (g l^{-1})	ln C_e	ln q_e
10	7.435	0.0150	496.52	2.006	−4.201
7.5	5.519	0.0116	477.06	1.708	−4.459
5.0	3.477	0.0089	390.88	1.246	−4.722
2.5	1.509	0.0058	260.94	0.412	−5.153
1.0	0.569	0.0025	225.86	−0.564	−5.984

Structural analysis was conducted using XRD patterns and Raman spectroscopy, while surface morphology was examined through SEM imaging.

Fig. 8a presents the X-ray diffraction (XRD) patterns of the ZnO and AZO thin film. The patterns reveal diffraction peaks corresponding to the (100) and (002) orientations of the ZnO wurtzite structure (JCPDS File No. 36-1451). The primary peaks of ZnO are located at $2\theta = 31.80°$ for (100) and $2\theta = 34.10°$ for (002). Notably, the (002) peak at 34.21° of AZO exhibits a clear shift compared to that of pure ZnO. This shift is consistent with the successful incorporation of Al^{3+} ions into the ZnO lattice, substituting for Zn^{2+} ions. Such substitution is known to cause lattice distortion because the ionic radius of Al^{3+} is smaller than that of Zn^{2+}, thereby altering the lattice parameters. Furthermore, the XRD pattern in Fig. 8a shows a preferential orientation along the (002) plane, indicated by dominant peak intensity of this peak. As reported in several studies, a strong (002) texture in ZnO-based materials is known to facilitate charge transfer along the c-axis, which could significantly contribute to the CM discussed in this work.[29,30]
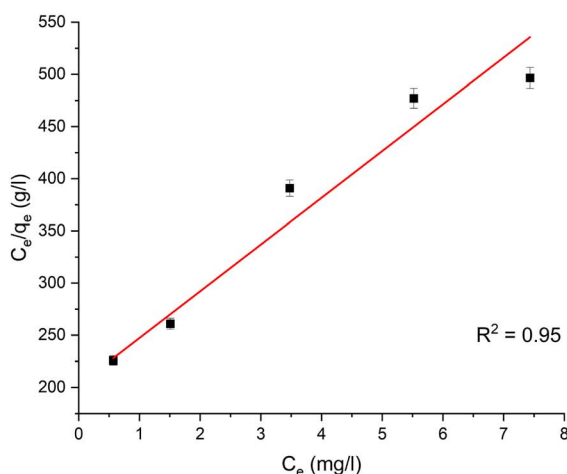
Fig. 8b presents the Raman spectra of the AZO and ZnO thin film. The ZnO thin film exhibits two characteristic vibrational modes: E_2 (high) at 440 cm^{-1} and A_1 (LO) at 575 cm^{-1}.[31] In contrast, the AZO substrate reveals two prominent peaks at 449 cm^{-1} and 560 cm^{-1}, both shifted relative to those of pure ZnO.[32] Similar with XRD patterns in Fig. 8a, these shifts can be attributed to the incorporation of Al^{3+} dopants into the ZnO crystal lattice, altering the lattice parameters. Similar observations were reported by A. Shah *et al.*, who demonstrated that Al doping induces a shift to higher wavenumber in the E_2 (high) mode is due to the substitution of Al^{3+} for Zn^{2+}.[31] Additionally, a study by Huyen Le Thi Minh *et al.* reported the appearance of a peak at 259 cm^{-1}, corresponding to the theoretically predicted silent B_1 mode at 261 cm^{-1}. This peak is attributed to defect formation in the AZO structure resulting from Al doping.[12] The substitution of Al^{3+} for Zn^{2+} not only modifies the vibrational characteristics of the material but also enhances the film's electrical conductivity. The increased free electron concentration facilitates charge transfer between the semiconductor and the sensing analytes, thereby amplifying the Raman signal through the CM mechanism.
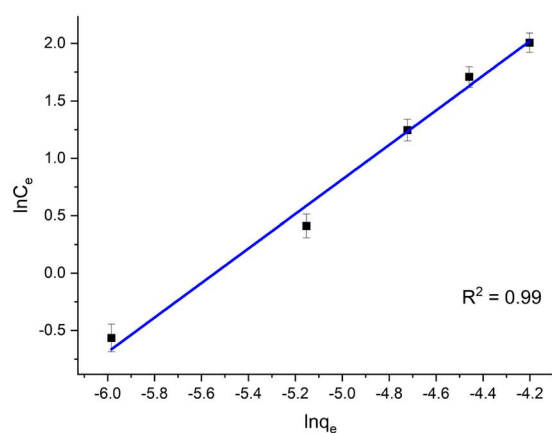
Based on the Raman analysis above, it can be concluded that the AZO substrate has successfully incorporated Al^{3+} into the ZnO crystal lattice, enhancing the film's conductivity and thereby supporting the Raman signal enhancement. Additionally, Al^{3+} doping induces defect levels, which further enhance CT in SERS.

The cross-sectional SEM image of the fabricated AZO substrate in Fig. 9a reveals a uniform AZO crystal growth with an approximate thickness of 1.64 μm. The surface image in Fig. 9b shows that the AZO substrate exhibits surface roughness, with porous cavities around 200 nm in diameter forming on the surface. These porous cavities enhance the adhesion of AgNPs and organic molecules, thereby contributing to the enhancement of the Raman signal.

3.3.2. Optical properties of AZO substrate. The PL spectrum of the AZO substrate is shown in Fig. 10a, obtained using an excitation wavelength of $\lambda_{ex} = 250$ nm. Gaussian

a)

b)

Fig. 7 (a) Graphs showing the relationship between C_e and q_e based on Langmuir's isotherm for MP. (b) Graphs showing the relationship between C_e and q_e based on Freundlich's isotherm for MP.
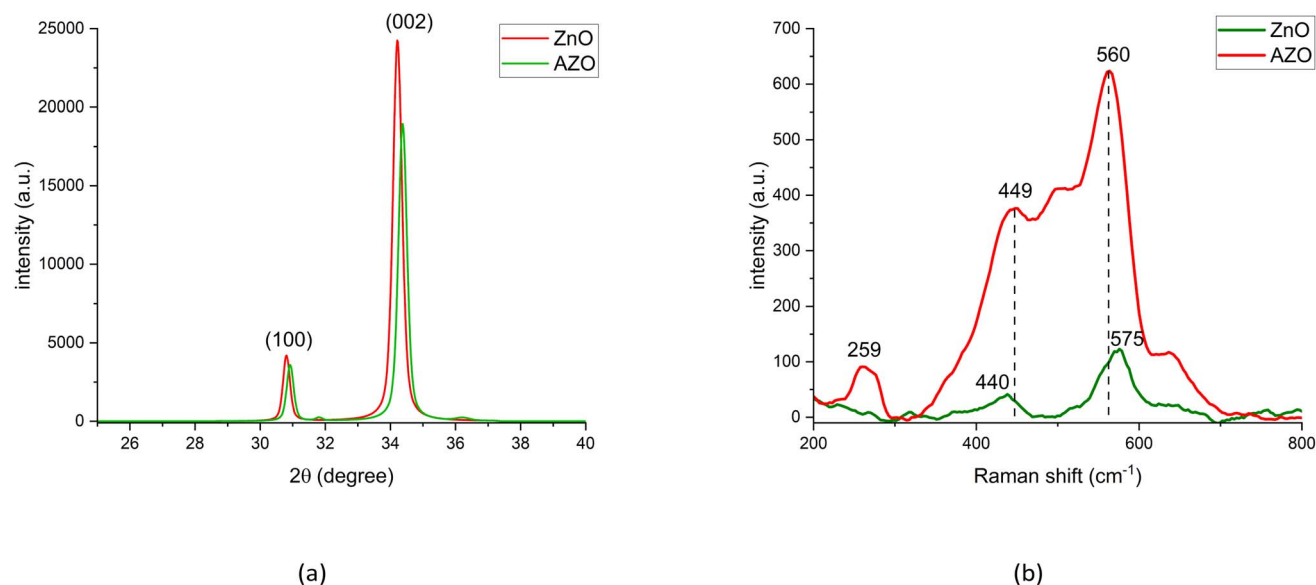
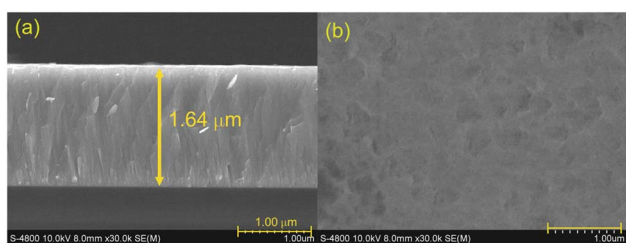Fig. 8 (a) XRD patterns of the ZnO and AZO thin film, (b) Raman spectrum of the ZnO and AZO thin film.

Fig. 9 (a) Cross-sectional SEM image of the AZO substrate, (b) surface SEM image of the AZO substrate.

deconvolution reveals five emission peaks at 372 nm, 389 nm, 401 nm, 436 nm, and 736 nm, corresponding to energy levels of 3.33 eV, 3.18 eV, 3.09 eV, 2.84 eV, and 1.68 eV, respectively.

Fig. 10b shows a column chart illustrating the contribution level of the emission peaks in the PL spectrum. The 3.33 eV peak (372 nm) accounts for 28.1% of the total emission and corresponds to the band-to-band transition of ZnO.[33–35] This transition occurs when electrons excited from the valence band (VB) to the conduction band (CB) recombine, emitting a photon consistent with the ZnO bandgap (E_g). The emission peaks at 389 nm (18.6%) and 401 nm (12.3%) are attributed to defect levels related to Zn vacancies (V_{Zn}), while the 436 nm peak (11.8%) corresponds to oxygen defects within the ZnO crystal lattice.[33–35] The 736 nm peak (29.1%) is linked to a complex transition involving Zn vacancies (V_{Zn}) and doubly ionized oxygen vacancies (V_0^{++}), as reported by Hua Jiang *et al.*[35] This emission region is particularly strong, indicating efficient CT pathways. Consequently, electrons can easily transition through these defect
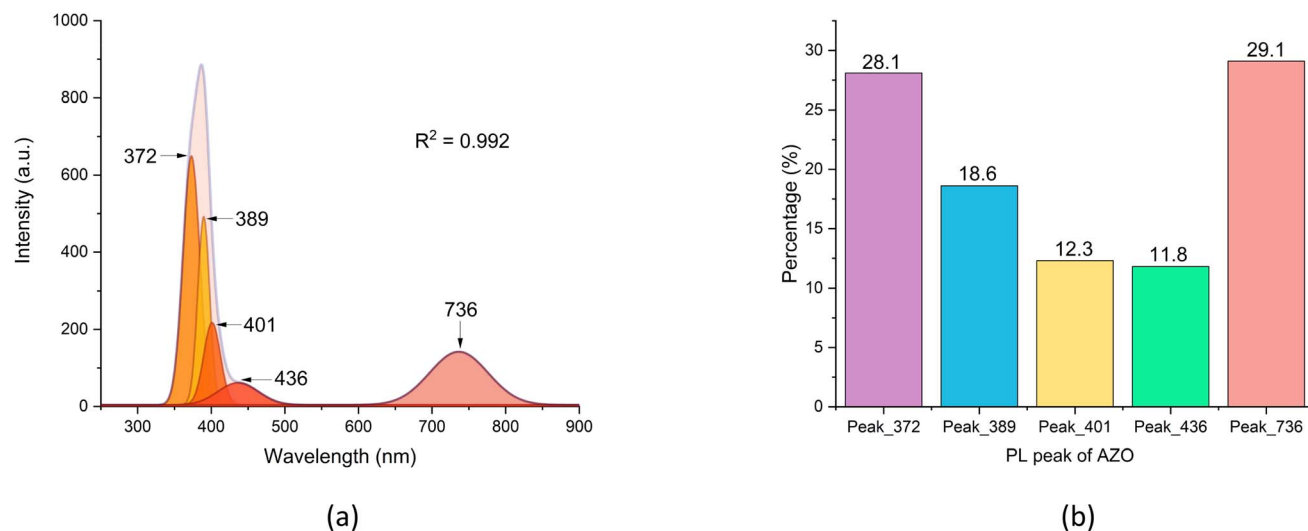

Fig. 10 (a) Gaussian deconvoluted PL spectrum of the AZO substrate, (b) bar charts illustrating the contribution of different component emissions to the total PL spectrum of the AZO substrate.

levels to reach the highest occupied molecular orbital (HOMO) of the organic molecule, thereby enhancing the SERS effect *via* the CT mechanism.

3.4. Determination of enhanced Raman signals of different analyte molecules on Ag/AZO SERS substrate

3.4.1. Evaluation of different SERS substrates with R6G molecules

3.4.1.1. Experimental setup for evaluating the CM contribution in SERS enhancement. To evaluate the CM contribution and the synergistic between EM and CM of SERS enhancement, five different SERS substrates were prepared for detecting R6G, a reference SERS probe. The AgNPs (sample Ag50) were collected by centrifugation. Specifically, 100 μL of Ag50 solution was aspirated and centrifuged, followed by the removal of 80 μL of the supernatant, leaving behind 20 μL of the concentrated AgNP solution at the bottom of an eppendorf tube. For each SERS substrate, measurements were performed in triplicate at multiple distinct locations on the sample. The results from these various locations were then averaged to obtain a representative value used for comparison with other samples (Table 4).

This setup allows a comparative analysis of the EM and CM contributions to SERS enhancement, providing insights into the role of CT as well as the synergistic interaction between the EM and CM in signal amplification.

Fig. 11 shows the characteristic peaks of the R6G at 609 cm^{-1}, 771 cm^{-1}, 1125 cm^{-1}, 1180 cm^{-1}, 1311 cm^{-1}, 1360 cm^{-1}, 1510 cm^{-1}, 1575 cm^{-1}, and 1650 cm^{-1}. The peak of 609 cm^{-1} is the C–C–C ring in-plane bending vibration. 771 cm^{-1} is the C–H out-of-plane bending vibration. 1125 cm^{-1} and 1180 cm^{-1} are the C–H in-plane bending vibrations. 1360 cm^{-1}, 1510 cm^{-1}, 1650 cm^{-1} are assigned to C–C stretching. 1311 cm^{-1}, 1575 cm^{-1} are N–H in-plane bend vibrations.[36]

3.4.1.2. The Raman signal intensities of R6G exhibit notable variations depending on the substrate. Sample SERS1 and SERS2 (without AgNPs): the Raman signal intensity at 609 cm^{-1} is relatively weak for both ZnO and AZO substrates. AZO shows a 1.61-fold increase in intensity compared to ZnO, likely due to the presence of Al doping, which enhances the CT effect. The improvement in AZO is attributed to electrons from the dopant

and defect levels, which facilitate the CT mechanism and contribute to slight Raman signal enhancement. This result clearly highlights the role of semiconductors as SERS substrates, even in the absence of noble metal nanoparticles like AgNPs.

Sample SERS3: a significant increase in intensity is observed compared to both ZnO and AZO alone, indicating that the AgNPs are present at an appropriate concentration, effectively enhancing the Raman signal through a strong EM.

Sample SERS4 and SERS5: both substrates exhibit higher Raman intensities compared to AgNPs on glass, confirming the synergistic effect of AgNPs and semiconductor substrates. The SERS5 shows the highest intensity at 609 cm^{-1}, surpassing SERS4. This indicates the cooperative enhancement effect of both CM and EM mechanisms, with the combination of AgNPs and the AZO semiconductor providing optimal signal enhancement.

As mention above, The EM relies on LSPR excitation in illuminated noble metal nanoparticles (*e.g.*, Ag, Au), generating intense local electromagnetic fields. Structures providing numerous such gaps, like the rough Ag/AZO SERS substrate shown in Fig. 12 with its uniform, high-density AgNPs distribution, act as effective platforms with abundant potential hot spots that strongly enhance the Raman signals of analytes adsorbed within them. Realizing such optimal nanostructures with high hot spot density is, however, highly fabrication-dependent. For instance, sputtering techniques often encounter difficulties in controllably depositing discrete, closely spaced spherical Ag nanoparticles, as increasing the amount of deposited Ag (*via* extended time or higher power) tends to form continuous metallic films instead of the discrete particle structures essential for effective hot spots. In contrast, the microwave synthesis combined with centrifugation method employed in this study can yield AgNPs that, upon deposition, form structures with a higher density of effective hot spots, consequently leading to more significant Raman signal enhancement through the EM mechanism.

From the comparison of the SERS substrates above, we selected the SERS5 sample to perform evaluations with the analytes R6G and MP.

Table 4 SERS substrate configurations

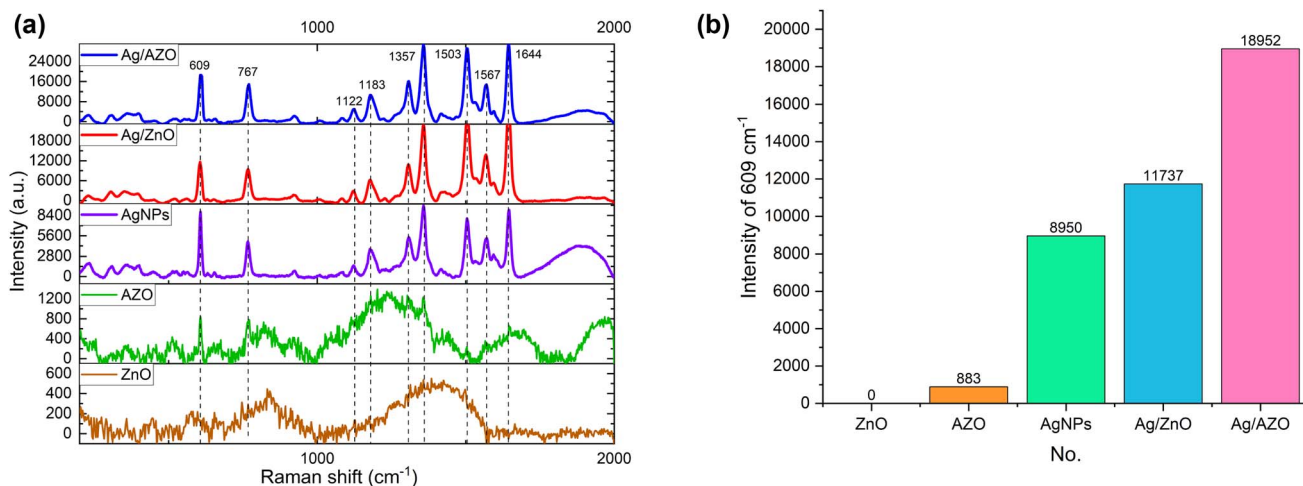| Sample	Practice method	Purpose of the substrate variations
SERS1	20 μL of 10^{-6} M R6G was directly dropped onto the surface of a ZnO substrate	Assess the Raman enhancement provided solely by the semiconductor substrates (ZnO and AZO), and evaluate the contribution of the CM to the overall enhancement
SERS2	20 μL of 10^{-6} M R6G was directly dropped onto the surface of an AZO substrate	
SERS3	AgNPs (sample Ag50) were mixed with 20 μL of 10^{-6} M R6G, allowed to interact for 1 hour, and then deposited onto a bare glass substrate	Evaluate the plasmonic enhancement (EM) provided by AgNPs in the absence of semiconductor influence
SERS4	AgNPs (sample Ag50) were mixed with 20 μL of 10^{-6} M R6G, allowed to interact for 1 hour, and then deposited onto an AZO substrate	Examine the combined effect of AgNPs with semiconductor substrates, highlighting the charge transfer contributions from AZO and ZnO, as well as the synergistic interaction between the EM and CM
SERS5	AgNPs (sample Ag50) were mixed with 20 μL of 10^{-6} M R6G, allowed to interact for 1 hour, and then deposited onto a ZnO substrate	

Fig. 11 (a) The Raman spectra of R6G at 10^{-6} M adsorbed onto different SERS substrates, including ZnO, AZO, AgNPs on glass, Ag/ZnO, and Ag/AZO, (b) a comparison of the SERS intensities at 609 cm^{-1} for R6G at 10^{-6} M adsorbed onto different substrates.
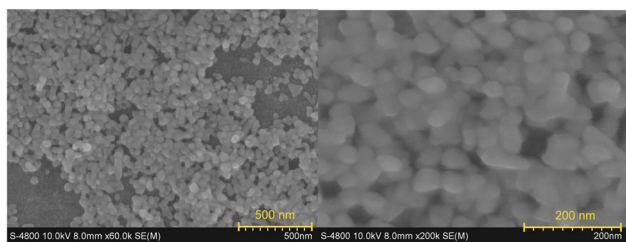

Fig. 12 The SEM image of Ag/AZO SERS substrate.

3.4.2. Detection of analyte molecules. In the following section, we evaluate the Ag/AZO SERS substrate using R6G and MP, to assess its detection capability and Raman signal enhancement capability. To do this, the analytes were prepared at various concentrations, and the sample preparation procedure for sample SERS5 (Section 3.4.1.) was followed.

3.4.2.1. SERS substrate evaluation with R6G. Fig. 13a presents the Raman spectra of R6G at concentrations ranging from 10^{-5} M to 10^{-14} M adsorbed onto an Ag/AZO SERS substrate. The characteristic peaks of R6G, particularly at 609 cm^{-1} and 1360 cm^{-1}, are clearly observed, demonstrating exceptional sharpness even at a concentration of 10^{-13} M. Notably, under 10^{-13} M, the 609 cm^{-1} peak disappears while the 1360 cm^{-1} peak persists. This observation aligns with the determined limit of detection (LOD) for R6G, which is based on the intensity of the 1360 cm^{-1} peak.

The exceptional sensitivity of this SERS substrate, capable of detecting R6G at extremely low concentrations, can be attributed to the specific interaction between R6G molecules and AgNPs. The adsorption of R6G onto AgNPs follows the Langmuir model, which describes monolayer adsorption. This indicates that R6G molecules bind to AgNPs in a specific orientation, forming a well-ordered layer. This oriented adsorption directly influences the Raman spectra, ensuring a highly consistent signal. Since the R6G molecules are

uniformly arranged and fixed in a specific orientation relative to the AgNPs, the characteristic peak ratios in the Raman spectra remain stable across a wide concentration range.

This study underscores the critical role of CM in SERS substrates. By fine-tuning the interaction between analyte molecules and plasmonic nanoparticles/semiconductor, it is possible to achieve exceptionally high sensitivity, pushing the boundaries of molecular detection to unprecedented levels.

The strong linear correlation ($R^2 = 0.990$) in Fig. 13b confirms the reliability of using the 609 cm^{-1} peak intensity for quantifying R6G concentration. This allows for accurate estimation of unknown R6G concentrations based on the Raman intensity, further demonstrating the high sensitivity and analytical capability of the Ag/AZO SERS substrate.

3.4.2.2. SERS substrate evaluation with MP. The preparation method ensures that MP molecules interact with AgNPs under similar conditions as R6G, allowing for a consistent comparison of SERS performance across different analytes and substrates. The MP solution was prepared with a volume of 20 μL mixed with 20 μL of Ag solution.

Fig. 14a presents the Raman spectra of MP with concentrations ranging from 100 ppm to 0.001 ppm. The spectrum reveals four characteristic peaks at 1156 cm^{-1}, 1282 cm^{-1}, 1586 cm^{-1}, and 1608 cm^{-1}, corresponding to the vibrational modes of C–O–C symmetric stretching, COO stretching, and C=O stretching.[37,38]

The analysis of the relationship between the intensity of the 1586 cm^{-1} peak and the MP concentration, as depicted in Fig. 14b, demonstrates a linear dependence within the concentration range of 100 ppm to 0.001 ppm. This strong correlation suggests that the Ag/AZO SERS substrate provides a reliable platform for detecting and quantifying MP at trace levels.

Among the characteristic peaks, the 1586 cm^{-1} peak remained sharp and stable across all concentrations. However, the relative intensities of the peaks varied slightly at different concentrations. This variation is attributed to the adsorption
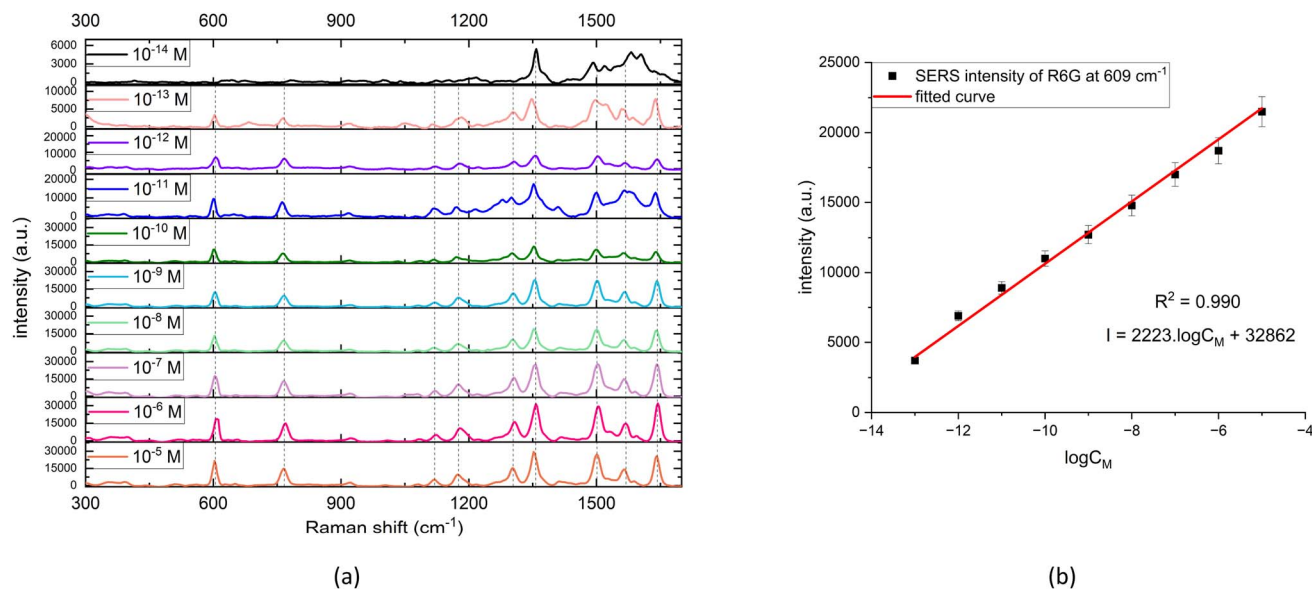
Fig. 13 (a) Raman spectra of R6G at a concentration from 10^{-5} M to 10^{-14} M on Ag/AZO SERS substrate. (b) The linear relationships of the peak intensity at 609 cm^{-1} and the logarithm of R6G concentrations in the range of 10^{-5} M to 10^{-14} M.
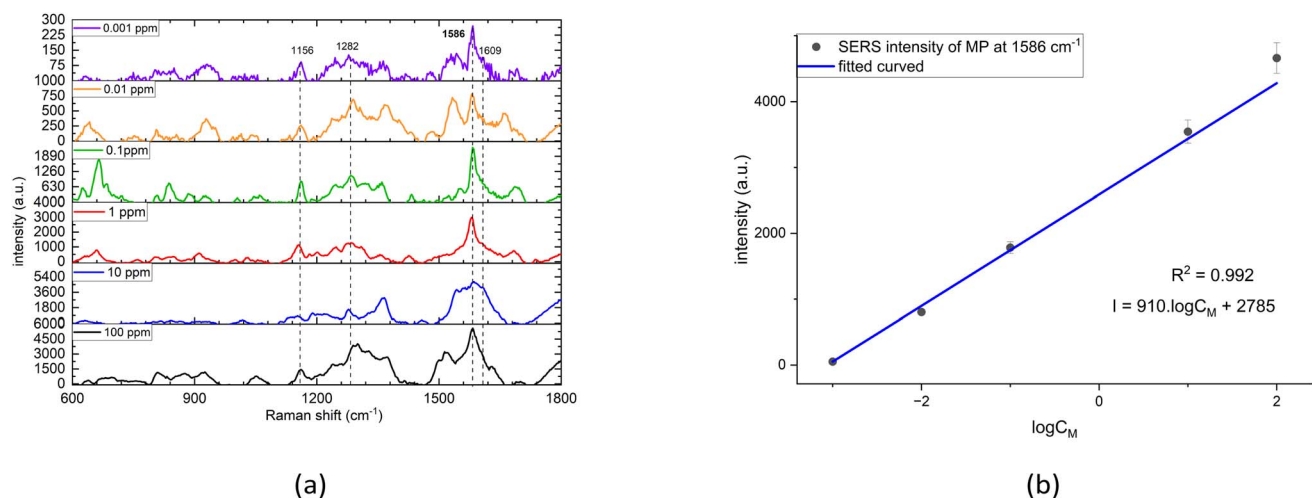

Fig. 14 (a) Raman spectra of MP at concentration ranging from 100 ppm to 0.001 ppm ($\sim 6.58 \times 10^{-9}$ M) on Ag/AZO SERS substrate. (b) The linear relationships of the peak intensity at 1586 cm^{-1} and logarithm of MP concentrations ranging between 100 ppm to 0.001 ppm ($\sim 6.58 \times 10^{-9}$ M).

behaviour of MP on AgNPs following the Freundlich model, which describes multilayer adsorption. As molecules attach to the AgNPs, changes in bonding occur, leading to variations in bond angles. The radicals bond to the AgNPs exhibit stronger interactions compared to others, resulting in fluctuations in peak intensity.

Furthermore, the 1282 cm^{-1} peak of MP in powder form is typically the most intense.[37,38] However, in this study, the 1586 cm^{-1} peak dominates across all samples. The change of these peaks can be attributed to the adsorption of the C=O group of MP molecules onto the AgNPs surface *via* coordination bonding (as illustrated in Fig. 15).[39] This interaction significantly affects the vibrations of the COO group, leading to

a notable decrease in its intensity. Consequently, the adsorption of MP on the AgNPs surface enhances charge transfer in the CM, further amplifying the Raman signal.

Below a concentration 0.001 ppm, the Raman signal of MP is no longer detectable. Therefore, 0.001 ppm ($\sim 6.58 \times 10^{-9}$ M) is determined as the limit of detection (LOD) of the Ag/AZO SERS substrate for MP molecules. This demonstrates the high sensitivity of the substrate, enabling the detection of MP at ultra-low.

3.4.2.3. Evaluation of the SERS substrate's EF for R6G and MP. In this section, we perform an evaluation of the enhancement factor (EF) of the SERS substrate towards the R6G analyte and MP. The SERS enhancement factor (EF) is calculated according to the following formula:[13]
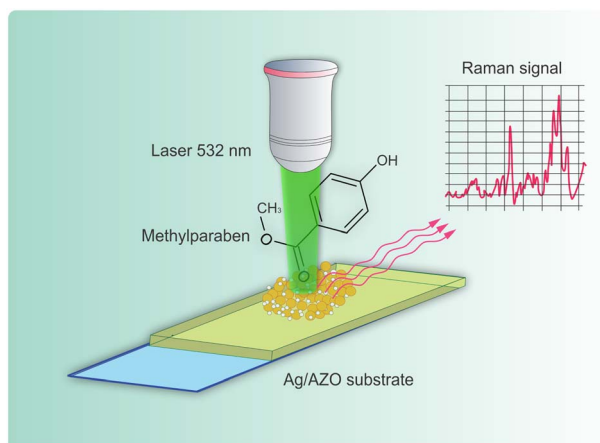
Fig. 15 The structure of the MP molecule and the adsorption of MP onto Ag nanoparticles *via* C=O group.

$$EF = \frac{I_{SERS}}{I_{bare}} \times \frac{N_{bare}}{N_{SERS}} \tag{9}$$

where I_{bare} and I_{SERS} correspond to the normal Raman intensity and SERS of analyte molecules, $N_{bare} = C_{bare} \times V$ is the average number of absorb molecules in the scattering volume, V, for the Raman (non-SERS) measurement, and $N_{SERS} = C_{SERS} \times V$ is the average number of molecules in the same scattering volume for the SERS experiments (Table 5).
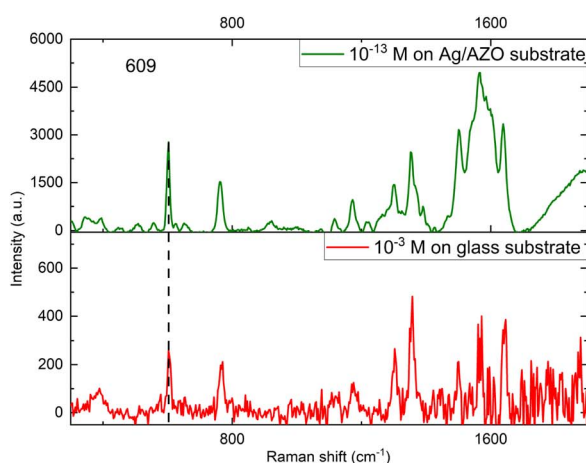
The results in Fig. 16 indicate that, using the same Ag/AZO SERS substrate, the EF for R6G is 5.98×10^4 times higher than

that of MP. This suggests that R6G exhibits a stronger interaction with the Ag/AZO substrate, likely due to its higher adsorption efficiency and charge transfer capability. The manner in which R6G and MP adsorb onto the surface of AgNPs is a crucial factor governing the intensity and characteristics of the resulting SERS spectra. The adsorption of R6G typically conforms to the Langmuir isotherm model, suggesting the formation of a monolayer on relatively homogeneous, specific adsorption sites on the AgNP surface. This implies that R6G binds strongly and assumes a favourable orientation on the surface, thereby maximizing its interaction with the localized enhanced electromagnetic field. This typically results in a very strong SERS signal that may reach saturation upon complete surface coverage. Conversely, the adsorption of MP onto AgNPs is often better described by the Freundlich isotherm model. This model suggests adsorption onto a heterogeneous surface with varying binding affinities and the potential for multilayer formation. This implies that only the MP molecules in direct contact with the Ag surface benefit substantially from the SERS enhancement, while subsequent layers experience significantly diminished enhancement. Consequently, although MP still yields a SERS signal, its intensity is generally lower than that of R6G. This reflects the different nature of its interaction and distribution on the silver nanoparticle surface.
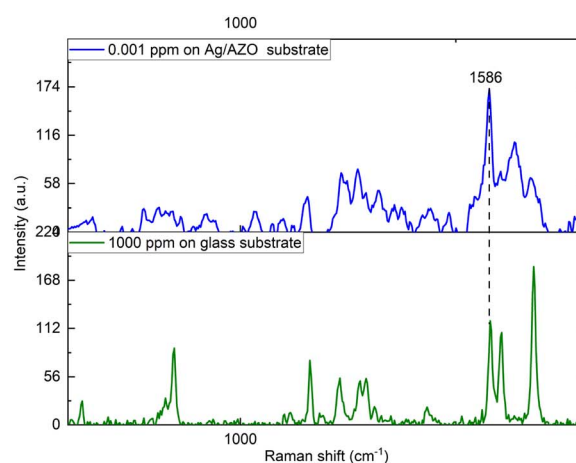
The reproducibility of the SERS substrate was evaluated by storing AZO substrates in a slide box with a silica gel desiccant at 27 °C, while the Ag50 solution was refrigerated at 2 °C. Before each use, the Ag50 solution was stirred for 30 minutes and centrifuged to obtain AgNPs. The Raman signal reproducibility

Table 5 The EF of analyte molecules on Ag/AZO substrate

Analyte molecules	The chosen peak at wave number (cm^{-1})	C_{SERS}	I_{SERS} (a.u.)	C_{bare}	I_{bare} (a.u.)	EF
R6G	609	10^{-13} M	2358	10^{-3} M	272	8.67×10^{10}
MP	1586	0.001 ppm ($\sim 6.58 \times 10^{-9}$ M)	175	1000 ppm	121	1.45×10^6

a)

b)

Fig. 16 (a) Raman spectra of R6G at 10^{-3} M on glass substrate and 10^{-13} M onto SERS substrate to calculate EF. (b) Raman spectra of MP at 1000 ppm on glass substrate and 0.001 ppm ($\sim 6.58 \times 10^{-9}$ M) onto SERS substrate to calculate EF.
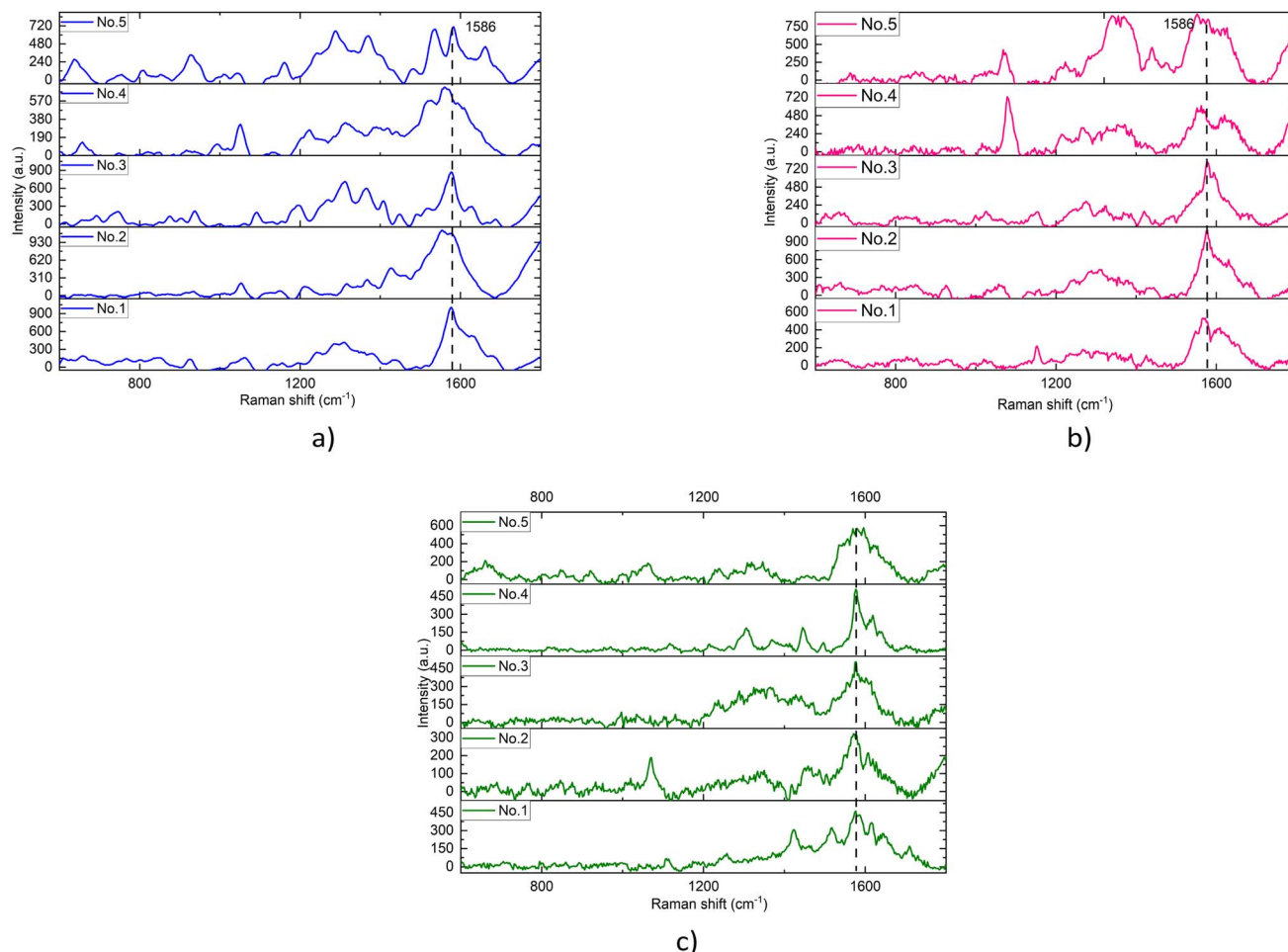
Fig. 17 Raman spectra of MP at five random positions with 0.01 ppm adsorbed on Ag/AZO substrate produced after (a) 1 month, (b) 2 months, and (c) 3 months.

for MP was assessed 1, 2, and 3 months after fabrication. At each time point, measurements were performed on three samples, focusing on the 1586 cm^{-1} peak due to its stability compared to other peaks.

Fig. 17a–c show the Raman spectra of MP after 1, 2, and 3 months, respectively. The results indicate that: After 1 month, the intensity at 1586 cm^{-1} had an average value of 845 a.u. with an RSD of 17.0%. After 2 months, the intensity decreased to 777 a.u., with an RSD of 19.4%. After 3 months, the intensity further declined to 478 a.u., and the RSD increased to 19.8%. The observed reduction in Raman intensity can be attributed to the oxidation of AgNO$_3$ over time under light and temperature exposure.[40,41] This oxidation promotes the formation of byproducts such as Ag$_2$O, which can interfere with the formation of AgNPs during centrifugation.[42] As a result, fewer AgNPs with the desired size are formed, leading to a decrease in hot spots and a corresponding reduction in Raman signal enhancement.

3.5. Propose the charge transfer scheme of CM of R6G, and MP on Ag/AZO substrate

In this section, we propose a CT scheme for CM of R6G and MP on the Ag/AZO substrate. Based on this model, we explain the

differences in the enhancement of the Raman signals for R6G and MP.

Premixing AgNPs with the analyte molecules (R6G and MP) before depositing them onto the AZO substrate enhances their adsorption onto the AgNPs. The formation of Schottky junctions between AgNPs and the AZO substrate plays a crucial role in CT dynamics. In the absence of external excitation, electron transfer does not occur from Ag, ZnO, or AZO to the organic molecules. PL spectroscopy reveals oxygen and zinc defect states at approximately −5.7 eV (E_{ss}), as shown in Fig. 10. These defect states and surface energy levels are fundamental to understanding the enhancement of the Raman signal. Raman spectra were obtained using a 532 nm laser (excitation energy ~2.33 eV). In ZnO, electrons in the valence band (VB) level can be excited to the E_{SS} level. From there, these electrons possess enough energy to transition to the conduction band (CB).

Fig. 18a and b illustrate the proposed CT mechanism for R6G and MP, respectively. For the R6G analyte, the CT process involves electron movement from the highest occupied molecular orbital (HOMO) to the Fermi level (EF) of the AgNPs, and subsequently to the lowest unoccupied molecular orbital
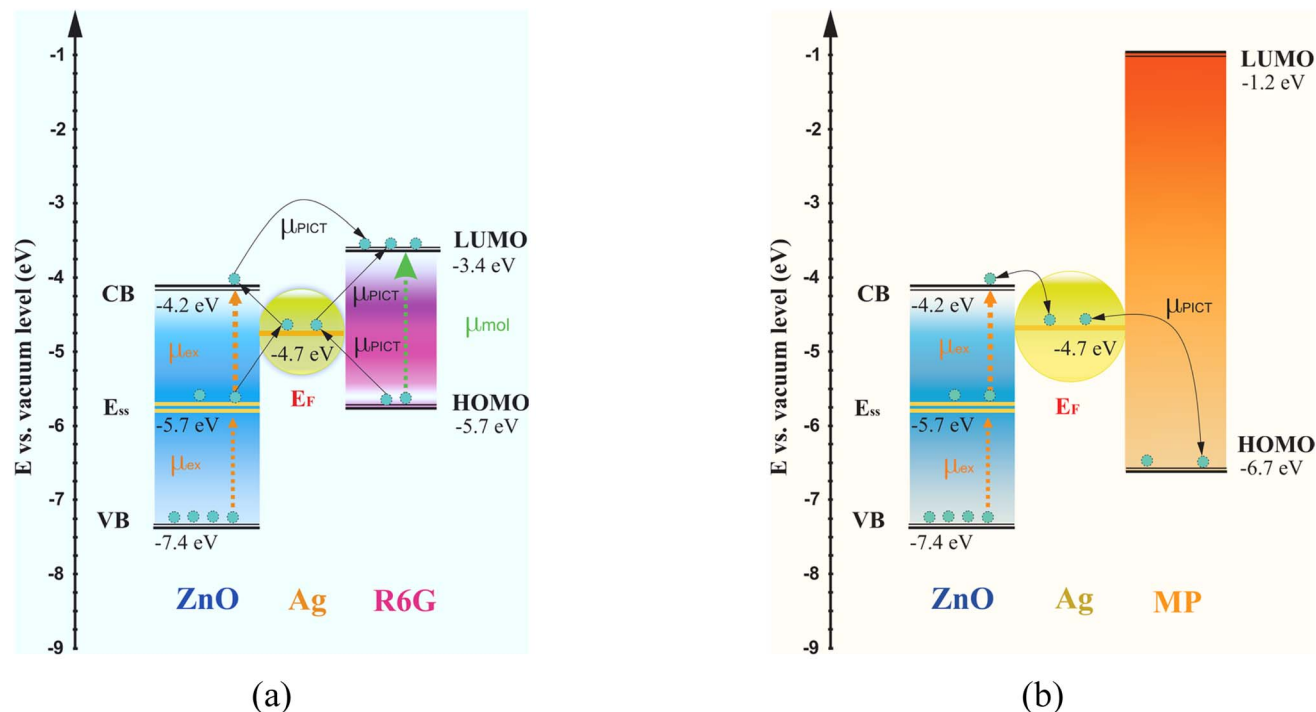
Fig. 18 (a) Charge transfer diagram of R6G and Ag/AZO substrate, (b) charge transfer diagram of MP and Ag/AZO.

(LUMO).[43] Additionally, electrons from the VB of ZnO can be excited to the E_{SS} defect level, then move to the EF of Ag and the CB of ZnO. From there, the electrons continue to transfer to the LUMO of the R6G molecule. Through these two pathways, the diagram effectively illustrates the proposed CT mechanisms (μ_{PICT}) based on studies of Raman enhancement mechanisms.[43,44] For the MP analyte, CT occurs solely through the movement of electrons from the HOMO of MP to the EF of the AgNPs and subsequently to the CB of ZnO. Since the CT mechanism of MP follows only this single pathway, the Raman spectrum of the MP analyte is more challenging to detect compared to that of the R6G analyte.

4. Conclusion

In this study, we fabricated a highly sensitive and stable Ag/AZO SERS substrate using DC magnetron sputtering for AZO deposition, along with microwave irradiation and centrifugation methods for AgNPs synthesis. Results indicated that a 50 mM $AgNO_3$ solution produced uniform AgNPs approximately 50 nm in size. AgNPs synthesized *via* these methods potentially create numerous hot spots on the rough AZO surface, enhancing the EM. The study also confirmed the CM's critical role, including molecular adsorption on AgNPs and CT between the AZO semiconductor film, AgNPs, and adsorbed molecules. Adsorption isotherm analysis revealed R6G's monolayer adsorption yielded stronger Raman signals compared to MP's multilayer adsorption. Furthermore, a CT pathway within the AgNPs-AZO-molecule system was proposed based on experimental data. Consequently, the fabricated SERS substrate demonstrated outstanding sensitivity through synergistic EM and CM

contributions, achieving an EF of 8.67×10^{10} and a LOD of 10^{-13} M for R6G, alongside an EF of 1.45×10^6 and an LOD of 0.001 ppm ($\sim 6.58 \times 10^{-9}$ M) for MP.

However, a limitation arises from differential molecular adsorption; inherent structural differences and unique analyte HOMO/LUMO levels critically affect interactions with AgNPs and CT dynamics at the interfaces, leading to molecule-dependent signal variations. Consequently, future directions include developing composite substrates, exploring material combinations, or employing binding agents to enhance analyte-nanoparticle adsorption for detecting a wider range of molecules.

Data availability

All data underlying the results are available as part of the article, and no additional source data are required.

Author contributions

Trong Vo Huu: investigation, measure, formal analysis, writing–original draft & editing. Vy Truong Tran Nhat: synthesize, measure, analyze. Mai Nguyen Xuan: measure. Hang Nguyen Thi Ngoc: measure. Long Nguyen Hoang: measure. Tuan Anh Dao: measure. Ke Nguyen Huu: review. Hung Le Vu Tuan: conceptualization, investigation, review & editing, supervision.

Conflicts of interest

There are no conflicts to declare.

Acknowledgements

References

1 M. Fleischmann, P. J. Hendra and A. J. McQuillan, *Chem. Phys. Lett.*, 1974, **26**, 163–166.

2 P.-Y. Sacré, E. Deconinck, T. De Beer, P. Courselle, R. Vancauwenberghe, P. Chiap, J. Crommen and J. O. De Beer, *J. Pharm. Biomed. Anal.*, 2010, **53**, 445–453.

3 L. Lan, Y. Gao, X. Fan, M. Li, Q. Hao and T. Qiu, *Front. Phys.*, 2021, **16**, 43300.

4 K. M. Naik and S. T. Nandibewoor, *Sens. Actuators, A*, 2014, **212**, 127–132.

5 O. Handa, S. Kokura, S. Adachi, T. Takagi, Y. Naito, T. Tanigawa, N. Yoshida and T. Yoshikawa, *Toxicology*, 2006, **227**, 62–72.

6 B. Saad, Md. F. Bari, M. I. Saleh, K. Ahmad and M. K. M. Talib, *J. Chromatogr. A*, 2005, **1073**, 393–397.

7 Y. Lin, C. Ferronato, N. Deng, F. Wu and J.-M. Chovelon, *Appl. Catal., B*, 2009, **88**, 32–41.

8 M. Liu, A. Bhandari, M. A. Haqqani Mohammed, D. R. Radu and C.-Y. Lai, *Appl. Nanosci.*, 2021, **2**, 242–256.

9 S. Cong, X. Liu, Y. Jiang, W. Zhang and Z. Zhao, *The Innovation*, 2020, **1**, 100051.

10 L. Chen, Y. Zhao, Y. Zhang, M. Liu, Y. Wang, X. Qu, Y. Liu, J. Li, X. Liu and J. Yang, *Colloids Surf. A Physicochem. Eng. Asp.*, 2016, **507**, 96–102.

11 Y. Ling, Y. Zhuo, L. Huang and D. Mao, *Appl. Surf. Sci.*, 2016, **388**, 169–173.

12 L. Yang, M. Gong, X. Jiang, Y. Chen, X. Han, K. Song, X. Sun, Y. Zhang and B. Zhao, *Colloids Surf. A Physicochem. Eng. Asp.*, 2016, **508**, 142–149.

13 L. Liu, H. Yang, X. Ren, J. Tang, Y. Li, X. Zhang and Z. Cheng, *Nanoscale*, 2015, **7**, 5147–5151.

14 T. Sakano, Y. Tanaka, R. Nishimura, N. N. Nedyalkov, P. A. Atanasov, T. Saiki and M. Obara, *J. Phys. D Appl. Phys.*, 2008, **41**, 235304.

15 S. M. Asiala, J. M. Marr, G. Gervinskas, S. Juodkazis and Z. D. Schultz, *Phys. Chem. Chem. Phys.*, 2015, **17**, 30461–30467.

16 N. H. Ke, N. H. Thanh, N. H. Long, D. A. Tuan and L. V. T. Hung, *J. Mater. Sci.: Mater. Electron.*, 2021, **32**, 27318–27332.

17 H. Le Thi Minh, L. Tran Thi, H. Kim Nhat, H. Nguyen Thi Anh, T. Dao Anh, T. Nguyen Huu, K. Nguyen Duy and H. Le Vu Tuan, *J. Mater. Sci.: Mater. Electron.*, 2023, **34**, 283.

18 L. T. Minh Huyen, N. T. Phuc, H. T. Doan Khanh and L. V. Tuan Hung, *RSC Adv.*, 2023, **13**, 9732–9748.

19 H. Le Thi Minh, L. Tran Thi, H. Kim Nhat, H. Nguyen Thi Anh, T. Dao Anh, T. Nguyen Huu, K. Nguyen Duy and H. Le Vu Tuan, *J. Mater. Sci.: Mater. Electron.*, 2023, **34**, 283.

20 H. Barani and B. Mahltig, *J. Clust. Sci.*, 2022, **33**, 101–111.

21 A. Sobczak-Kupiec, D. Malina, Z. Wzorek and M. Zimowska, *Micro Nano Lett.*, 2011, **6**, 656–660.

22 R. Borah and S. W. Verbruggen, *Colloids Surf. A Physicochem. Eng. Asp.*, 2022, **640**, 128521.

23 N. Kh. Abdalameer, K. A. Khalaph and E. M. Ali, *Mater. Today: Proc.*, 2021, **45**, 5788–5792.

24 P. Hildebrandt and M. Stockburger, *J. Phys. Chem.*, 1984, **88**, 5935–5944.

25 A. Tripathi, E. D. Emmons, A. W. Fountain, J. A. Guicheteau, M. Moskovits and S. D. Christesen, *ACS Nano*, 2015, **9**, 584–593.

26 R. Saadi, Z. Saadi, R. Fazaeli and N. E. Fard, *Korean J. Chem. Eng.*, 2015, **32**, 787–799.

27 I. Mohammed, C. C. Afagwu, S. Adjei, I. B. Kadafur, M. S. Jamal and A. A. Awotunde, *Oil Gas Sci. Technol.*, 2020, **75**, 77.

28 I. T. Sugiarto, Isnaeni and K. Y. Putri, *J. Phys. Conf. Ser.*, 2017, **817**, 012047.

29 Q. Zhang, N. Li, J. Goebl, Z. Lu and Y. Yin, *J. Am. Chem. Soc.*, 2011, **133**, 18931–18939.

30 F. P. Jose, S. R. Achari, M. K. Jayaraj and A. A. Sukumaran, *J. Electroanal. Chem.*, 2021, **901**, 115769.

31 X. Liang and C. Wang, *Appl. Phys. Lett.*, 2020, **116**, 043903.

32 A. Shah, M. Ahmad, Rahmanuddin, S. Khan, U. Aziz, Z. Ali, A. Khan and A. Mahmood, *Appl. Phys. A*, 2019, **125**, 713.

33 M. A. Mahadik, Y. M. Hunge, S. S. Shinde, K. Y. Rajpure and C. H. Bhosale, *J. Semicond.*, 2015, **36**, 033002.

34 Q. Hou, F. Meng and J. Sun, *Nanoscale Res. Lett.*, 2013, **8**, 144.

35 H. Jiang, Y. Lu, X. Rong, S. Han, P. Cao, Y. Zeng, W. Xu, M. Fang, W. Liu and D. Zhu, *J. Electron. Mater.*, 2020, **49**, 4537–4543.

36 C. Wu, E. Chen and J. Wei, *Colloids Surf. A Physicochem. Eng. Asp.*, 2016, **506**, 450–456.

37 N. Vijayan, R. Ramesh Babu, M. Gunasekaran, R. Gopalakrishnan and P. Ramasamy, *J. Cryst. Growth*, 2003, **256**, 174–182.

38 S. Krishnamoorthi, G. N. Kasinathan, G. Paramasivam, S. N. Rath and J. Prakash, *ACS Omega*, 2023, **8**, 46628–46639.

39 S. Miljanić, A. Dijanošić and I. Matić, *Spectrochim. Acta, Part A*, 2015, **137**, 1357–1362.

40 H. I. Badi'ah, F. Seedeh, G. Supriyanto and A. H. Zaidan, *IOP Conf. Ser. Earth Environ. Sci.*, 2019, **217**, 012005.

41 Md. N. Haque, S. Kwon and D. Cho, *Korean J. Chem. Eng.*, 2017, **34**, 2072–2078.

42 J. Liu, Z. Wang, Y. Meng, C. Chen, Q. Chen, Y. Wang, S. Dou, X. Liu and N. Lu, *Talanta*, 2023, **258**, 124408.

43 S. Cong, X. Liu, Y. Jiang, W. Zhang and Z. Zhao, *The Innovation*, 2020, **1**, 100051.

44 J. R. Lombardi and R. L. Birke, *J. Phys. Chem. C*, 2014, **118**, 11120–11130.